

Electronic Supplementary Information

Synthesis of branched gold nanoparticles with tunable Near-InfraRed Localized Surface Plasmon Resonance using a zwitterionic surfactant for the seed-growth method

Piersandro Pallavicini, Giuseppe Chirico, Maddalena Collini, Giacomo Dacarro, Yuri Antonio Diaz Fernandez, Alice Donà, Laura D'Alfonso, Andrea Falqui, Stefano Freddi, Brigida Garofalo, Alessandro Genovese, Laura Sironi and Angelo Taglietti*

S1. TEM images of gold nanoparticles (seeds)

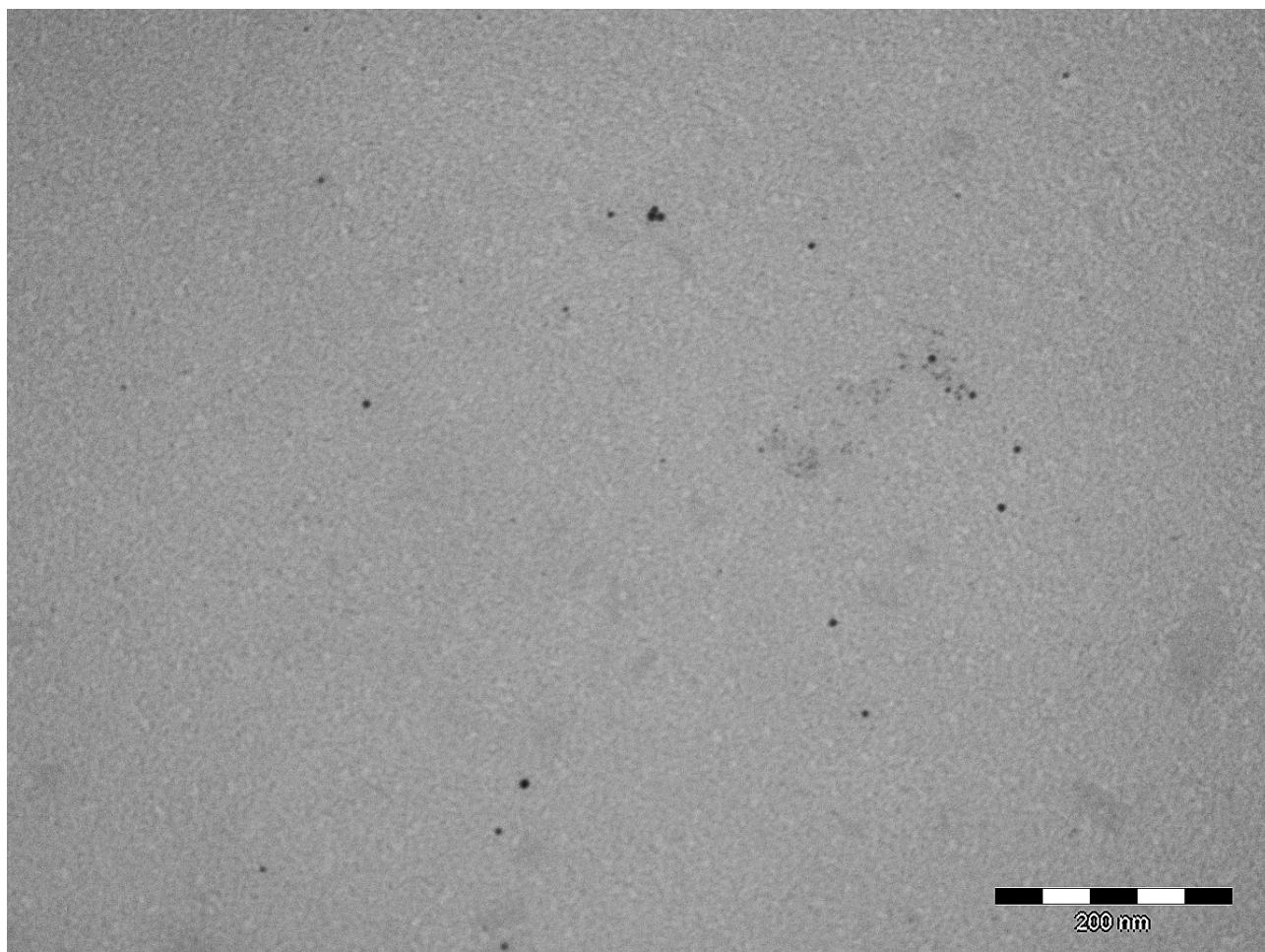


Figure S1, A

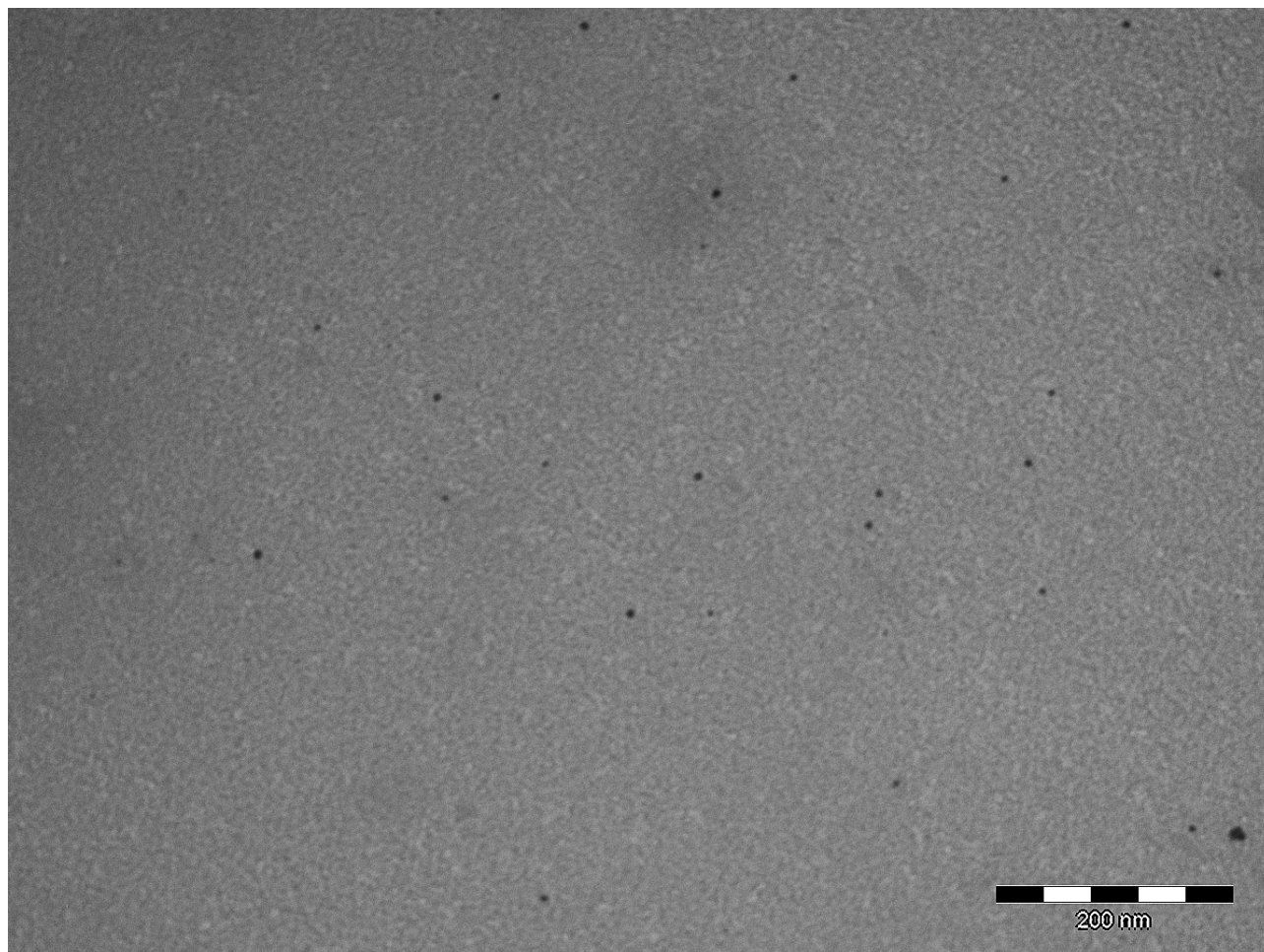


Figure S1, B

Figure S1 A and B: TEM images of NP from a seed solution obtained by mixing 5 mL of $5 \cdot 10^{-4}$ M $\text{HAuCl}_4 \cdot 2\text{H}_2\text{O}$ with 5 mL 0.20 M LSB in water, and by adding 600 μL of NaBH_4 0.010 M.

Preparation of samples for TEM images: a seed solution (concentrations as described in the main text) was dilute 1:100 in water, deposited on nickel grids (300 mesh) covered with a Parlodion membrane and observed with a Jeol JEM-1200 EX II instrument.

S2. Dynamic Light Scattering.

S2.a Solutions of LSB (LSB micelles).

Solutions of Laurylsulphobetaine (LSB, N-dodecyl-N', N''-dimethyl-3-ammonio-1-propane-sulphonate) were prepared in water at increasing concentrations from 0.2 to 0.6 M. The scattering experiments have been performed on a home made setup [Chirico et al. 1999] that uses a He-Ne laser (Nec, 50 mW, $\lambda = 633$ nm, vertical polarization) and a digital acquisition and correlator board by ISS (ISS, inc, Urbana, IL). The sample is lodged in a cylindrical cell kept at $T = 24^\circ\text{C}$.

The AutoCorrelation Function (ACF) of the intensity of the light scattered at the angle $\theta = 90^\circ$ can be fit to a single exponential decay according to the relation:

$$G(t) = \langle I \rangle^2 (1 + f^2 \exp[-2DQ^2t]) = \langle I \rangle^2 (1 + f^2 |g^{(1)}(t)|^2) \quad (\text{A1})$$

where Q is the scattering vector, $Q = 4\pi n \sin(\theta/2)/\lambda \cong 3.49 \times 10^{10} \text{ cm}^{-2}$. The translational diffusion coefficient D is then translated into the hydrodynamic radius, R_h , by means of the Stokes-Einstein relation:

$$D = \frac{K_B T}{6\pi\eta R_h} \quad (\text{A2})$$

In the above equations η and n are the viscosity and the refraction index of the solution, $T = 297.15$ K, is the solution temperature, f (Eq.1) is the signal/noise ratio typically $\cong 0.03$.

The ACFs reported in Fig.S2 indicates clearly that the relaxation time increases with the LSB concentration. Indeed the average hydrodynamic radius changes from $R_h \cong 1.6$ nm at $[\text{LSB}] = 0.2$ M, to $R_h \cong 3$ nm for $[\text{LSB}] = 0.6$ M, with a linear trend.

Table S1: micelles hydrodynamic

| [LSB] [M] | R_h [nm] |
|-----------|----------------|
| 0.2 | 1.6 ± 0.12 |
| 0.3 | 2.1 ± 0.2 |
| 0.4 | 2.3 ± 0.2 |
| 0.5 | 2.6 ± 0.2 |
| 0.6 | 3 ± 0.2 |

Table S1. Average hydrodynamic radii of micelles in solutions as obtained from polarized VV dynamic light scattering.

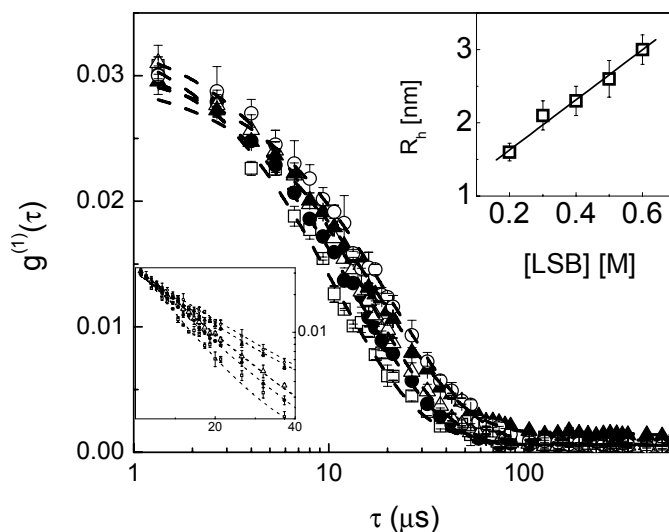


Figure S2. ACFs of the light scattered by the LSB micelle solutions. The symbols refer to [LSB] = 0.2 M (open squares); [LSB] = 0.3 M (filled circles); [LSB] = 0.4 M (open triangles); [LSB] = 0.5 M (filled triangles); [LSB] = 0.6 M (open circles). The dashed lines are the best fit of Eq.1 to the data. A small baseline has been added to the data fitting and is probably due to residual dust contribution to the scattering intensity. The top inset shows the linear trend of the R_h as a function of the LSB concentration. The bottom inset shows the ACFs in log-linear scale.

S2b. Dynamic light scattering of the NPs solutions.

The scattering of the solutions of the NPs has been measured through a vertical polarizer, i.e. parallel to the direction of the polarization of the laser light. In this case two exponential decays are needed to fit the data with relaxation times of the order 10 and 200 μs approximately (see Fig.S3). The presence of the faster component is taken as an evidence of the polarizability anisotropy of the NPs. In the view of the TEM analysis, the anisotropy of the polarizability is probably entirely due to the shape anisotropy of the NPs. The two relaxation components are then ascribed to the rotational and the translational diffusion of the NPs. According to the TEM image analysis the shape of the NPs may vary from spherical to branched and no clear cylindrical symmetry can be pointed out. The polarizability of the particle is in general a rank two tensor and can be diagonalized to give three eigenvalues that have the meaning of the polarizability along three orthogonal axes in the particle frame of reference. For sake of simplicity, we assume here that we can define in the NP a direction along which the polarizability (α_{\parallel}) of the electrons is much larger than in the other two orthogonal directions ($\alpha_{\perp} \ll \alpha_{\parallel}$). Within this assumption, the intensity autocorrelation function may be written in the form [Berne&Pecora 1976]:

$$G(t) = \langle I \rangle^2 \left(1 + f^2 \exp[-2DQ^2t] \left(\langle \alpha \rangle^2 + \frac{4}{45} (\alpha_{\parallel} - \alpha_{\perp})^2 \exp[-6\Theta t] \right) \right) \quad (\text{A3})$$

In the above expression, α indicates the average excess polarizability of the NP, α_{\parallel} is the polarizability along the long axis and α_{\perp} indicate the polarizabilities along the shorter axes (whose mutual difference with respect to α_{\parallel} can be neglected). The translational, D , and the tumbling rotational, Θ , diffusion coefficients can be used to derive the average hydrodynamic radius of the NP. The amplitudes of the two exponential components are instead used to estimate the degree of shape anisotropy as detailed hereafter. The experimental ACFs are fit then to a trial equation of the type: $G(t) = \langle I \rangle^2 (1 + Ae^{-\Gamma_R t} (1 + Re^{-\Gamma_T t}))$.

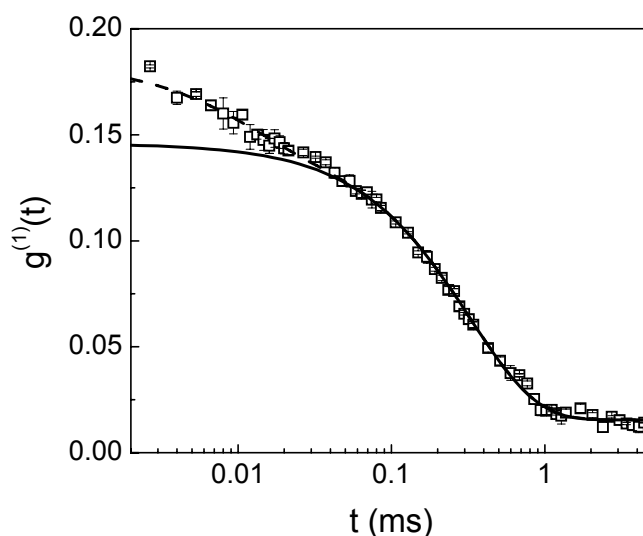


Figure S3. ACF of the light scattered by a solution of NPs prepared at $[\text{LSB}] = 0.2 \text{ M}$ observed through a polarizer whose axis is parallel to the polarization direction of the excitation beam (vertical). The dashed line is the best fit to the function $G(t) = \langle I \rangle^2 (1 + Ae^{-\Gamma_R t} (1 + Re^{-\Gamma_T t}))$ (Eq. A3). The solid line represent the translational component of the ACF. A small baseline accounts for the presence of larger aggregates as also indicated by the TEM analysis.

We assume that the anisotropy along a particle axis is proportional to the length of the axis and therefore:

$$\begin{aligned} \alpha_{\parallel} &\div L \\ \alpha_{\perp} &\div D \\ \alpha &\div \frac{1}{3}(L + 2D) \end{aligned} \tag{A4}$$

The ratio of the amplitudes of the translational to the rotational exponential components

obtained from the best fit, R_{fit} , is then given by:

$$R_{fit} = \frac{4}{45} \frac{(\alpha_{\parallel} - \alpha_{\perp})^2}{\alpha^2} = \frac{4}{45} \frac{\delta_{\alpha}^2}{\langle \alpha \rangle^2} \quad (\text{A5})$$

From Eq.A5 it is straightforward to derive the (effective) axial ratio, D/L , as:

$$\frac{L}{D} = 3 \left(\frac{2\delta_{\alpha}}{3\langle \alpha \rangle} - 1 \right) \left(1 - \frac{\delta_{\alpha}}{3\langle \alpha \rangle} \right)^{-1} \quad (\text{A6})$$

The best fit values of the ratio $R_{fit} = \frac{4}{45} \frac{\delta_{\alpha}^2}{\langle \alpha \rangle^2}$ are shown in Fig.3C of the main text and reported here in Table S2 together with the estimates of the axial ratios, L/D . The comparison to the L/B (length/base) values measured on the branches of asymmetric NP (type C objects, TEM_C in Table S2) and on the branches of nanostars (type B objects, TEM_B in Table S2) from TEM images indicates that the analysis reported here underestimate the shape anisotropy. This fact is expected since the axial ratio values are measured on the single branches on the TEM images, while Eq.A6 makes use of an overall polarizability anisotropy.

Table S2: DDLS amplitude analysis.

| [LSB] [M] | R_{fit} | $R_{h,T}$ [nm] | $R_{h,R}$ [nm] | $(L/D)_{A6}$ | $(L/B)_{TEM_C}$ | $(L/B)_{TEM_B}$ |
|-----------|-----------|----------------|----------------|--------------|------------------|------------------|
| 0.20 | 1.8±0.2 | 24±2 | 21±3 | 5.5±0.9 | 6.9±0.8 | 3.9±0.6 |
| 0.35 | 1.9±0.2 | 29±2 | 28±4 | 6.2±0.9 | 7.5±0.8 | 4.8±1.5 |
| 0.45 | 2.2±0.3 | 21±3 | 27±3 | 8.9±3.0 | 8.1±1.2 | 4.4±0.7 |
| 0.50 | 2.4±0.2 | 19±3 | 27±3 | 13.2±5.0 | 12.4±2.0 | |
| 0.60 | 2.4±0.2 | 21±3 | 25±3 | 13.6±5.0 | 7.8±3.7 | |

The best fit values of the ratio $R_{fit} = \frac{4}{45} \frac{\delta_{\alpha}^2}{\langle \alpha \rangle^2}$ are obtained from the analysis of the ACFs measured through a vertical polarizer. The hydrodynamic radius, $R_{h,T}$, is obtained from the slower relaxation rate (Γ_T) and Eq.A2. The hydrodynamic radius, $R_{h,R}$, is obtained from the faster relaxation rate (Γ_R) and Eq.A7. The ratios $(L/D)_{A6}$ are estimated from Eq.A6. The ratios $(L/D)_{TEM}$ are estimated from the analysis of the TEM images (see main text) on the C and B families of NPs (see main text).

From the translational relaxation component (Γ_T in the fitting function) we can derive the average hydrodynamic radius of the NPs according to Eq. A2. The best fit values, reported in table A2, indicate that the average encumbrance of the NPs is not changing with the

concentration of the LSB surfactant, though a marked increase in the anisotropy is observed through the $R_{fit} = \frac{4}{45} \frac{\delta_{\alpha}^2}{\langle \alpha \rangle^2}$ parameter.

Finally, regarding the information that can be obtained from the rotational relaxation rate, $\Gamma_R = 6\Theta$, we observe that to the first approximation we can estimate an average hydrodynamic radius from the relation:

$$\Theta = \frac{K_B T}{8\pi\eta R_{h,R}^3} \quad (\text{A7})$$

From Eq.A7 a very rough estimate of the overall encumbrance can be done, reported in Table S2, that, however, appears to be consistent with the estimate obtained from the analysis of the translational relaxation rate. The average values of the hydrodynamic radii obtained from the analysis of the translational and rotational components of the ACFs are in fact: $\langle R_{h,T} \rangle = 22.8 \pm 4$ nm and $\langle R_{h,R} \rangle = 26 \pm 3$ nm.

An more refined analysis of the rotational relaxation component can be done according to a number of relations. We assume here the formulation given by Tirado and Garcia de la Torre for the rotational diffusion coefficient of a rod:

$$\Theta = \frac{3K_B T}{\pi\eta L^3} \left[\ln\left(\frac{L}{D}\right) + \sigma \right] \quad (\text{A8})$$

$$\sigma = -0.662 + 0.917 \frac{D}{L} - 0.05 \left(\frac{D}{L}\right)^2$$

From the measurement of the rotational diffusion coefficient, $\Theta = \Gamma_R / 6$, and of the axial ratio, obtained above from the amplitudes of the two components of the ACFs, we can gain an additional estimate of the long and short axes of the effective ellipsoid with which we have approximated the NPs.

Tables S3. Estimates of the long and short effective axes of the NPs.

| LSB [M] | DDLS | | | | | TEM | |
|---------|--------------|----------------|----------|------------|------------|----------------|----------------|
| | $(L/D)_{A6}$ | Θ [kHz] | σ | L_R [nm] | D_R [nm] | L_{TEM} [nm] | B_{TEM} [nm] |
| 0.20 | 5.5±0.9 | 16.6 ± 3 | -0.497 | 65±4 | 12±2 | 55±3 | 8.0±0.8 |
| 0.35 | 6.2±0.9 | 6.9 ± 0.4 | -0.515 | 89±2 | 14±2 | 65±5 | 8.8±0.6 |
| 0.45 | 8.9±3.0 | 8.1 ± 0.4 | -0.559 | 91±1 | 10±4 | 61±2 | 7.5±1.1 |
| 0.50 | 13.2±5.0 | 8.2 ± 0.5 | -0.593 | 97±2 | 7.3±3 | 99±5 | 8.0±1.2 |
| 0.60 | 13.6±5.0 | 10.0 ± 1 | -0.595 | 92±3 | 6.7±2 | 64±9 | 8.2±3.7 |

The table reports the comparison of the estimate of the sizes of the axes of the NPs obtained from TEM and from DDLS analysis. The estimates of the long (L_R) and short (D_R) axes are obtained from the rotational diffusion coefficient Θ according to Eq.A8.

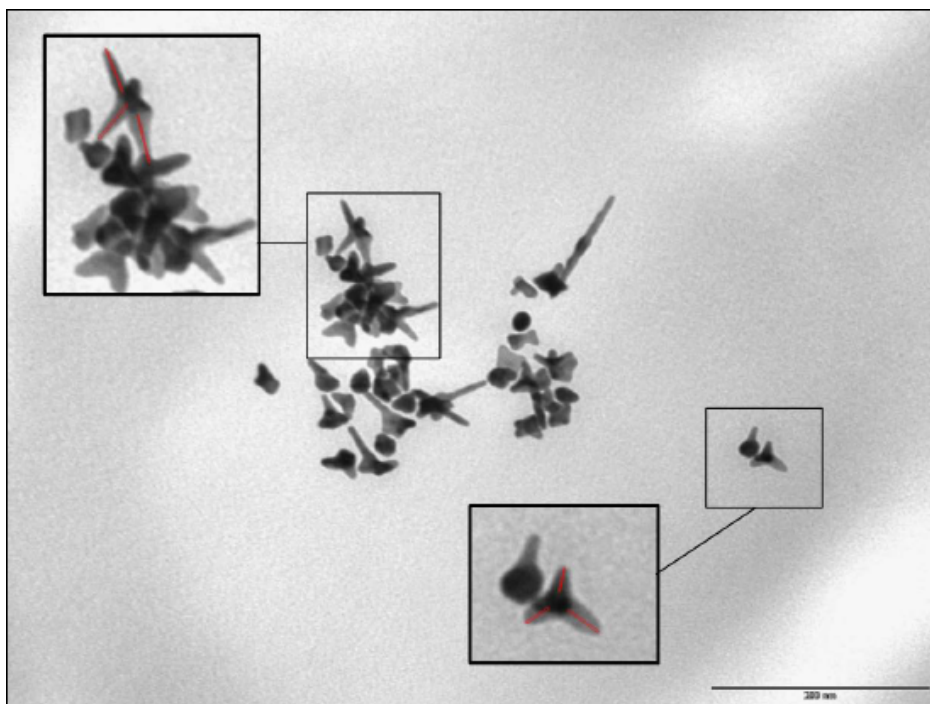
When trying to compare the values of length of the long and short axes of the NPs obtained

from DDLS and from TEM, one should consider that in the analysis of the TEM images, the lengths are taken on the single branches while in the assumptions made for the analysis of the DDLS ACFs we have described the whole NP as revolution ellipsoid. In this sense the overestimation of the length of the long axis observed in Table S3, can be understood and the DDLS data can be considered consistent with the TEM data.

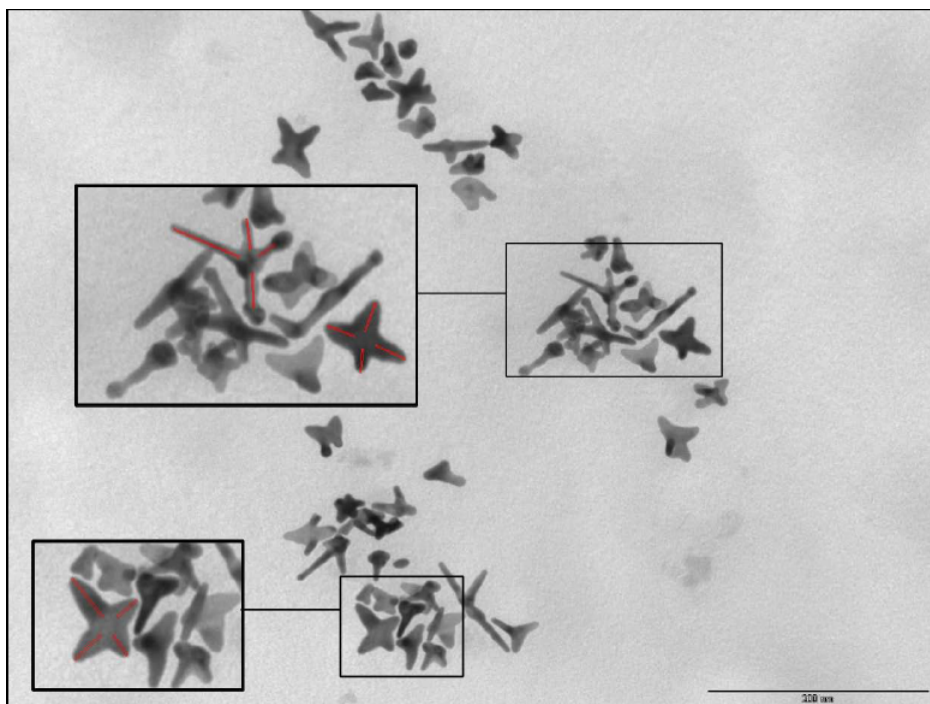
References:

1. Chirico, G; Beretta, S.; Baldini, G. *J. Chem. Phys.* (1999) 110: 2297-2304.
2. "Dynamic Light Scattering: With Applications to Chemistry, Biology, and Physics", Bruce J. Berne and Robert Pecora. 1976, Dover, N.Y. (USA), Ch. 7.
3. Garcia de la Torre, J.; Lopez Martinez, M. C.; Tirado, M. M. *Biopolymers* (1984), 23, 611-615.
4. Tirado, M. M.; Garcia de la Torre, J. *J. Chem. Phys.* 1979, 73, 1986-1993.
5. Tirado, M. M.; Lopez Martinez, M. C.; Garcia de la Torre, J. *J. Chem. Phys.* 1984, 81, 2047-2052.

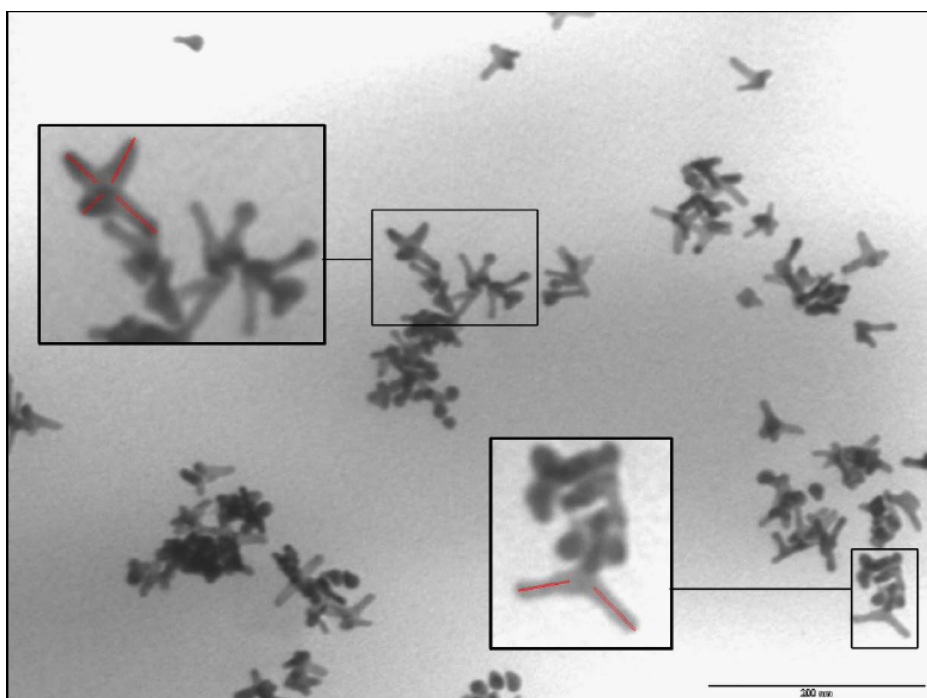
S3. TEM Images. TEM images obtained on dispersions of nanoobjects from growth solutions prepared with different LSB concentrations. As an example of the branch length calculation, some areas of the images are zoomed and the branch length evidenced in red. Dimension bar: 200 nm in all images



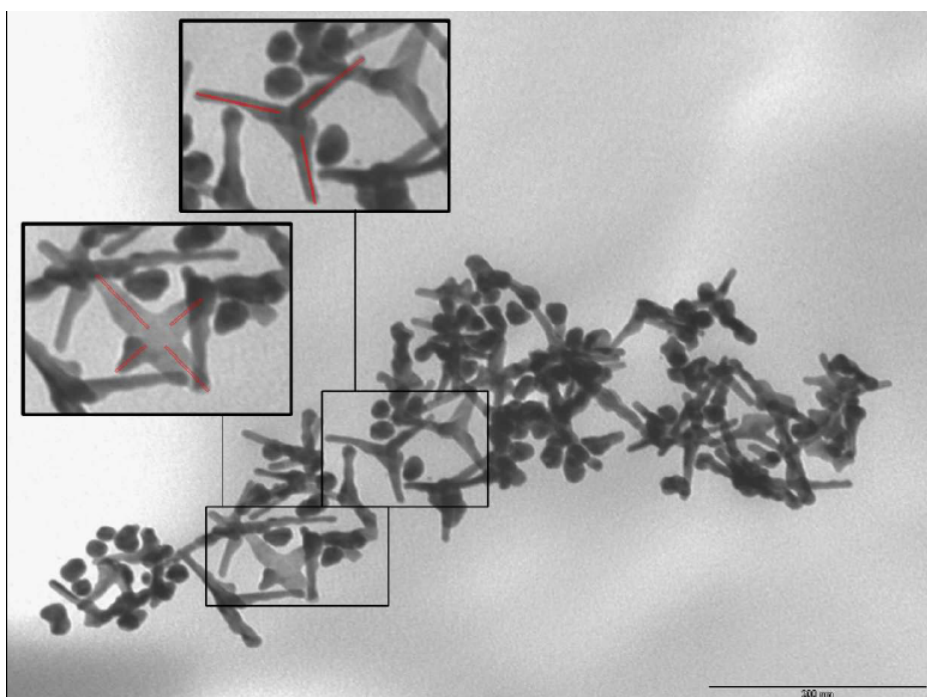
0.2 M LSB



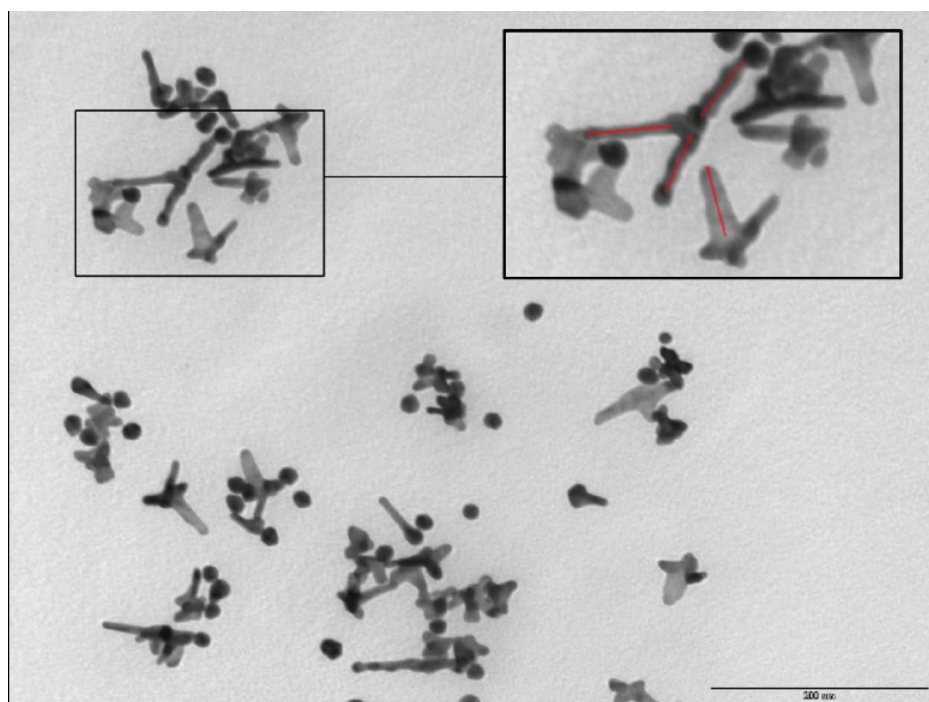
0.35 M LSB



0.45 M



0.5 M



0.6 M

S4. PEG₂₀₀₀-SH functionalization

Four 10 mL nanoobjects dispersions (D04_a, D04_b, D04_c, D04_d) were obtained using 0.4M LSB to prepare the growth solution, using the reactant concentrations described in the main text. Each dispersion was ultracentrifuged (13000 RPM for 20 min) the supernatant solution was removed and the obtained pellet was redissolved in 10 mL of bidistilled water. The obtained clear dispersions obtained from were then treated with 1.0-1.1 mg of PEG₂₀₀₀SH polymer, respectively (Iris Biotech, MeO-PEG-SH, MW:2000Dalton), corresponding to ~ 1:10 Au/PEG₂₀₀₀SH molar ratio, with respect to the total starting Au moles. The four samples were allowed to react at 25 °C on a reciprocating stirrer for 2 hours. A 10 nm red shift of the LSPR was observed (see Figure S4)

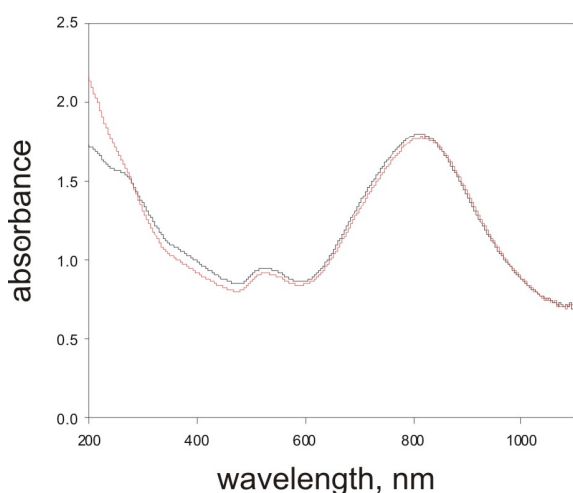


Figure S4. Black: UV-Vis spectrum of the starting nanostar dispersion. Red: UV-Vis spectrum after treatment with PEG₂₀₀₀SH

The samples were then ultracentrifuged and the supernatant solution was analyzed for unreacted thiol content, according to the Ellman procedure [C.K. Riener, G. Kada, H.J. Gruber, *Anal. Bioanal. Chem.*, **2002**, 373, 266-276]. To carry out the test we have built a calibrating curve with PEG₂₀₀₀SH in the 10⁻⁶-10⁻⁴ M range. Moreover, as the Ellman test is based on the measurement of the absorbance of 5-thio-2-nitrobenzoic acid at 412 nm, we measured the residual absorbance of any nanoobject eventually remained in solution after centrifugation (i.e. the UV-Vis spectrum of the supernatant solution before Ellman treatment) and subtracted it to the spectrum measured after the addition of the Ellman reagents.

From the concentration of free PEG₂₀₀₀SH determined by the Ellman test and the added PEG₂₀₀₀SH concentration we calculated the % of PEG thiol bound to the nano-objects, as shown in Table S4.1

Table S4.1. Free, bound and % of bound PEG₂₀₀₀SH on nano-objects dispersions obtained with LSB as the surfactant

| | PEG free(mol/L) | PEG bound (mol/L) | % bound PEG |
|------------------|-----------------------|-----------------------|-------------|
| D04 _a | 1.22*10 ⁻⁵ | 3.78*10 ⁻⁵ | 76% |
| D04 _b | 1.56*10 ⁻⁵ | 3.94*10 ⁻⁵ | 72% |
| D04 _c | 9.52*10 ⁻⁶ | 4.05*10 ⁻⁵ | 81% |
| D04 _d | 8.63*10 ⁻⁶ | 4.14*10 ⁻⁵ | 83% |

Average % bound PEG₂₀₀₀SH = 78% (±5)

To compare these results with the grafting of PEG₂₀₀₀SH on Au nanorods, we have synthesized gold NR according to the the same procedure and concentrations described in the main text, but using CTAB instead of LSB. We stress that this is the procedure described in ref 4b, leading to gold NR with AR < 4.5, and that the total quantity of gold is identical. In our case, we prepared four Au NR dispersion with this method (DNR_{a-d}, LSPR in the 760-765 nm range), then we treated them with PEG₂₀₀₀SH in the same quantities and with the same procedure described for our asymmetric nano-objects ($\Delta\lambda$ of ~ 10 nm to the red was observed in all cases). The Ellman test was used (same calibrating curve, same corrections) to calculated the % of bound PEG. The results are summarized in Table S4.2, evidencing a significantly lower % of bound PEG.

Table S4.2. Free, bound and % of bound PEG₂₀₀₀SH on nanorods dispersions obtained with CTAB (cetyltrimethylammonium bromide) as the surfactant

| | PEG free (mol/L) | PEG bound (mol/L) | % bound PEG |
|------------------|-----------------------|----------------------|--------------|
| DNR _a | 4.62*10 ⁻⁵ | 3.8*10 ⁻⁶ | 7.6% |
| DNR _b | 3.53*10 ⁻⁵ | 1.5*10 ⁻⁵ | 29.2% |
| DNR _c | 3.72*10 ⁻⁶ | 1.3*10 ⁻⁵ | 26.0% |
| DNR _d | 4.29*10 ⁻⁶ | 7.1*10 ⁻⁶ | 14.2% |

Average % bound PEG₂₀₀₀SH = 19 % (±10)

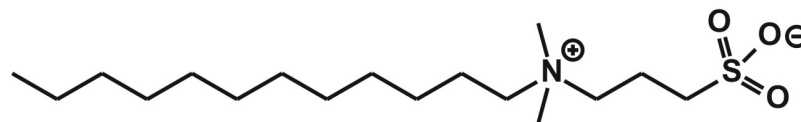
Reaction with PEG2000-SH produces coated nanoobjects stable to more than 4 centrifugation/redissolution cycles in water, resistant to Phosphate Saline Buffer and capable of phase transfer in CH₂Cl₂.

S5. Table with the population and dimensions of the different objects typologies

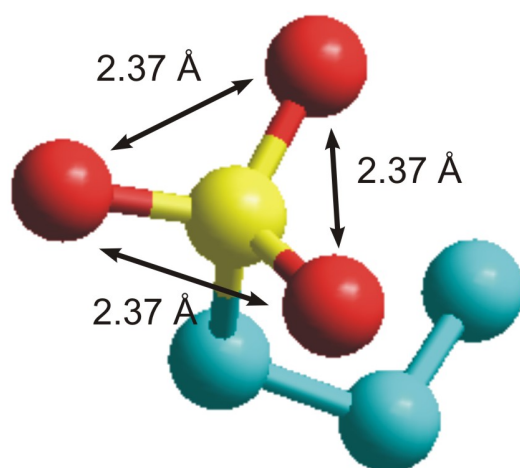
| [LSB] | Spheres (type A) % | Stars (type B) % | Branched (type C) % |
|--|----------------------------|--|---|
| 0.20 M (sample of spectrum in Figure 2A) | 13 | 37.6 L = 35.8 ± 1.9 nm B = 9.1 ± 1.3 nm | 49.4 L = 54.5 ± 3.0 nm B = 8.0 ± 0.8 nm |
| 0.35 M (sample of spectrum in Figure 2B) | 9.6 | 47.1 L = 41.0 ± 10.9 nm B = 8.5 ± 1.5 nm | 43.3 L = 65.4 ± 5.3 nm B = 8.7 ± 0.3 nm |
| 0.45 M (sample of spectrum in Figure 2C) | 10.8 | 30.4 L = 38.7 ± 5.0 nm B = 8.7 ± 0.7 nm | 58.8 L = 60.9 ± 1.9 nm B = 7.5 ± 1.1 nm |
| 0.50 M (sample of spectrum in Figure 2D) | 28 | 2 | 70 L = 98.9 ± 5.1 nm B = 7.9 ± 1.2 nm |
| 0.60 M ^a | 34 | 36 L = 39.9 ± 4.7 nm B = 11.4 ± 1.9 nm | 30 L = 64.3 ± 11.1 nm B = 8.2 ± 3.7 nm |

^a calculated on TEM images obtained after centrifugation and resuspension in water of the solution corresponding to Figure 2E spectrum. This was necessary as the high concentration of LSB caused deformation of the Parlodion membrane on the Ni grids

S6. Formula sketch of laurylsulphobetaine and molecular model of a R-SO₃⁻ moiety



LSB, laurylsulphobetaine



Molecular model obtained by semiempirical method AM1 with the HyperChem 7.5 program

S7. Analysis of the samples, yield calculation

S7A. Thermo Gravimetric Analysis (TGA). The samples were prepared by drying overnight, under vacuum, the solid pellets obtained from nanostar syntheses (using LSB solutions in the 0.2-0.4M range) after centrifugation at 13000 rpm for 30 minutes and removal of the supernatant. The solid product was in the 4-5 mg range for 10ml of starting solution.

The solid obtained was placed on an alumina crucible in a variable amount (from 3mg to 5 mg). The TGA measurements were performed using an instrument SDT Q600 from TA, equipped for working from room temperature to 1500°C. The TGA curves were recorded under nitrogen flux (15mL/min) heating the sample from 25°C to 1200°C. Over this temperature the inorganic residual mass varied less than hundredth of mg. A typical TGA curve is shown in Figure S7a.

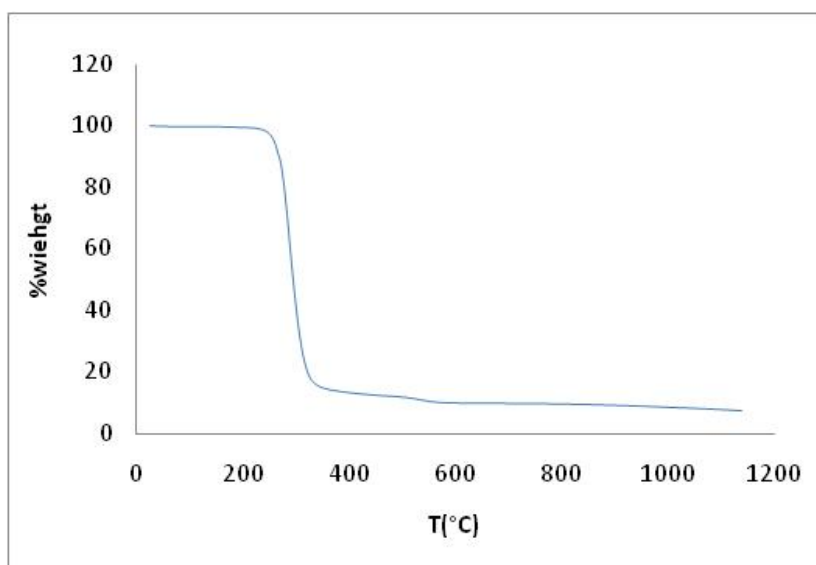


Figure S7a. TGA profile of typical nano-objects sample

S7B. Yield calculation. TGA profiles showed a sharp step-decrease jump starting at 250°C, typical of thermal decomposition of organic matrixes, i.e. the surfactant LSB, that is the main component in the solid samples (it has to be remembered that decantation of the supernatant after centrifugation yields a solid pellet that is still thoroughly wet of the starting solution, in which the surfactant concentration was 2 order of magnitude larger than gold concentration). This weight loss was in the 88-92%. The remaining 12-8% weight of the starting 4-5 mg of solid is assigned to Au, with eventually Ag traces.

Direct evaluation of the nano-objects composition was performed by EDS-STEM analysis (Energy Dispersive Spectrometry by Scanning Transmission Electron Microscopy). For the experimental details, see next paragraph S9). Several EDS spectra were acquired in STEM on small regions (i.e., with area of few square nanometers), each containing a single nano-object. The results indicate that gold is $\geq 90\%$, Ag being the only other element detected.

According to this, a minimum of 0.288 mg and a maximum of 0.540 mg Au is contained in the solid samples isolated from syntheses. The starting quantity of gold in the growth solutions is always 0.985 mg (0.005 mmol, from 5.0ml \times 0.001 M $\text{HAuCl}_4 \cdot 2\text{H}_2\text{O}$; the Au contribution from the seed solutions is negligible). The calculated yields are thus in the range 29.2-54.8 %.

S7C. Scanning Electron Microscopy – Energy Dispersion Microanalysis. The samples for SEM analysis were prepared by centrifugating (13000 rpm, 30 minutes) 10 mL of nanoobjects solutions prepared with 0.2-0.4 M LSB. The supernatant was removed and the remaining solid pellet was dried under vacuum overnight.

From this protocol, about 5mg per 10ml of starting solution were typically obtained. The solid was placed on a bi-adhesive graphite slide fixed on the aluminum sample-holder. The typical golden-coating for SEM preparations was avoided in order to allow the quantitative determination of the original amount of gold, sulfur, chloride (and eventually silver) in the sample. The SEM analysis was performed using a EvoMA10 microscope fabricated by Zeiss. The experiments were carried out using a 20kV and the beam current of 50 mA. The composition of the samples was determined by Energy Dispersion Microanalysis (EDS), using an INCA Energy 350 X Max detector from Oxford Instruments. Cobalt standard was used for the calibration of the quantitative elementary analysis.

Several determinations were made for each sample at different points of the sample holders. For each point a topographical image was recorded and the EDS microanalysis was performed. A typical set of recorded data is shown at fig S5. A, where the characteristic peaks of gold, sulfur, silver and chloride are labeled. The microanalysis determination were reproducible inside the same sample and between different synthesis batches within the 20%. Quantitative determination of carbon and oxygen was not possible due to the interference of the sample holder. The average elementary composition was dominated by sulphur, in agreement with the excess quantity of LSB remained after sample preparation. Besides S, Au (and a minor contribution from Ag) were found. The most important data from this analysis is the negligible quantity of chloride, whose signal was so low that accurate quantification was not possible.

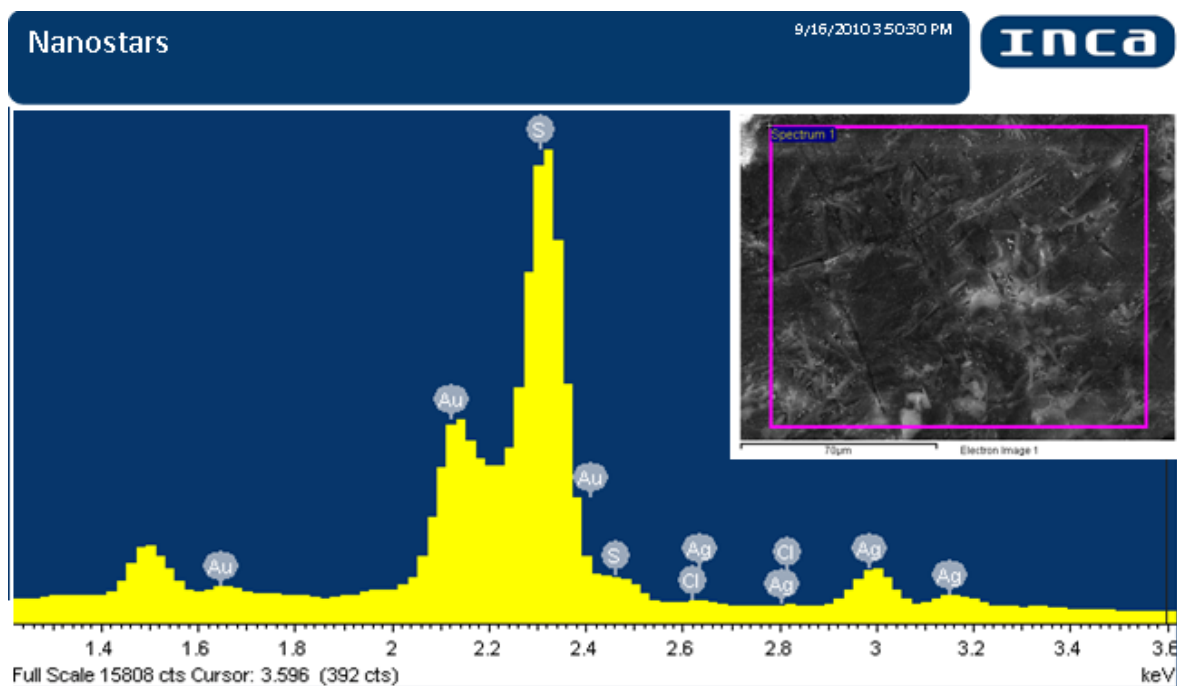


Figure S7b. Microanalysis data from a typical nano-objects sample showing the X-rays signals of the detected/labeled elements . Inset: topographic image on the sample region analyzed

S8. Electron diffraction pattern

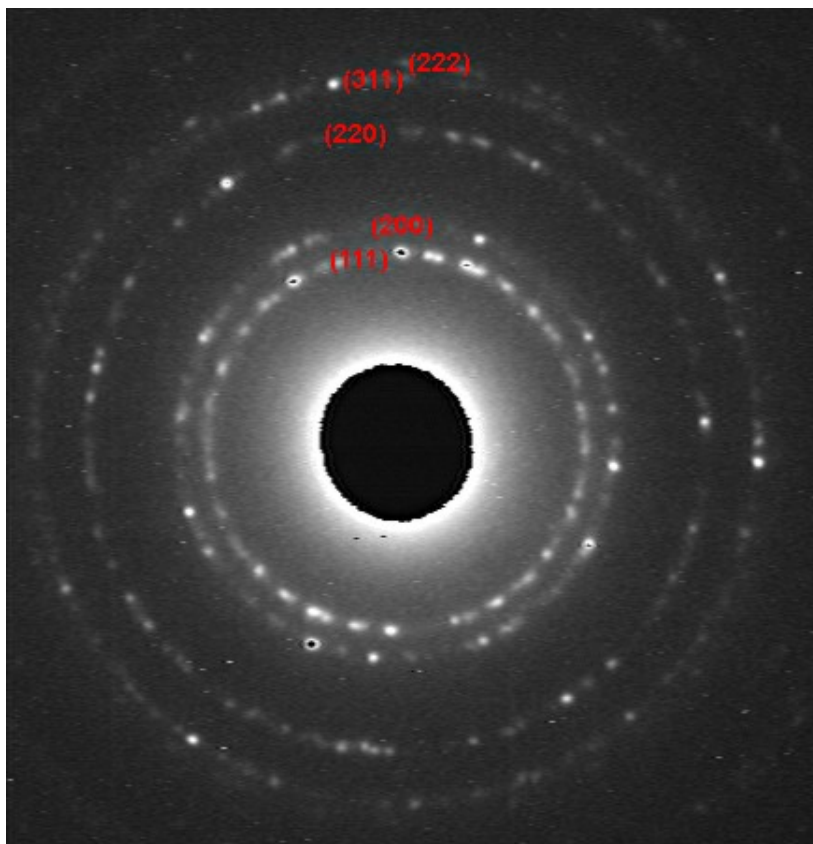


Figure S8. Electron diffraction pattern, obtained with a TEM instrument from a preparation with 0.4M LSB. The different diffraction rings (corresponding to the different Au lattice sets) were indexed and the indexes reported in the image.

S9. High Resolution TEM images (HRTEM). HRTEM imaging, as well as EDS-STEM analysis, was performed by using a Jeol JEM 2200FS TEM/STEM working at 200 kV. The microscope was equipped with a field emission electron source, a Jeol Si(Li) EDS spectrometer and a CEOS corrector of objective lens spherical aberration. The ultimate point resolution achieved was 0.9 Å in HRTEM mode and 2.1 Å in STEM mode. In the case of STEM measurements, an electron probe of 1 nm in size was also used.

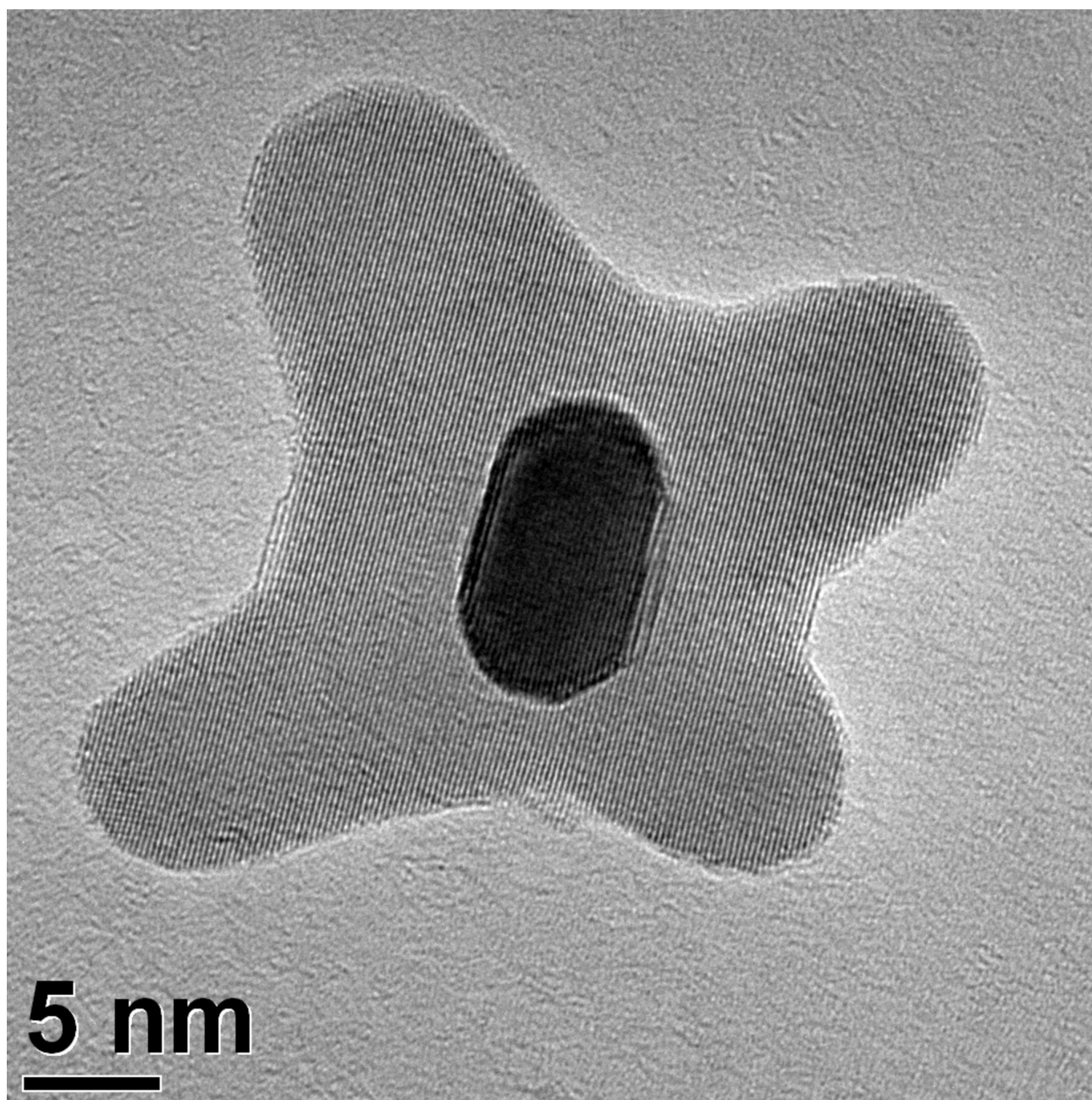


Figure S9a. Full image of a monocrystalline nanostar, i.e. typology **B** objects (a detail is reported in the main text as Figure 1vi). The darker spot in the centre is a fifth branch pointing towards the observer. A sixth branch may be hidden behind the structure

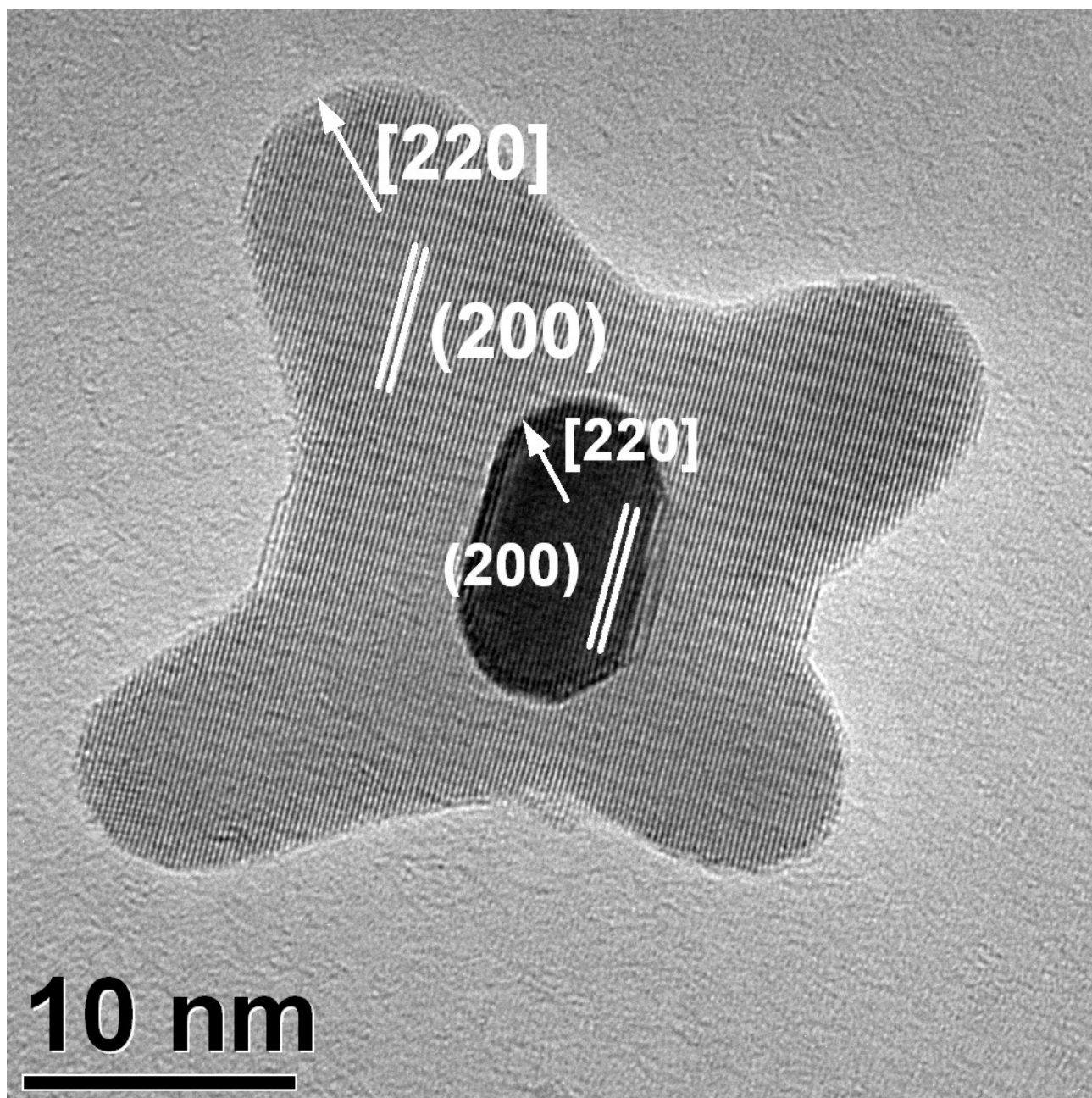


Figure S9b. Same as Figure S9a, with evidenced growth directions. The arm pointing out from the image plane (*i.e.*, towards the reader) has grown along the [200] direction

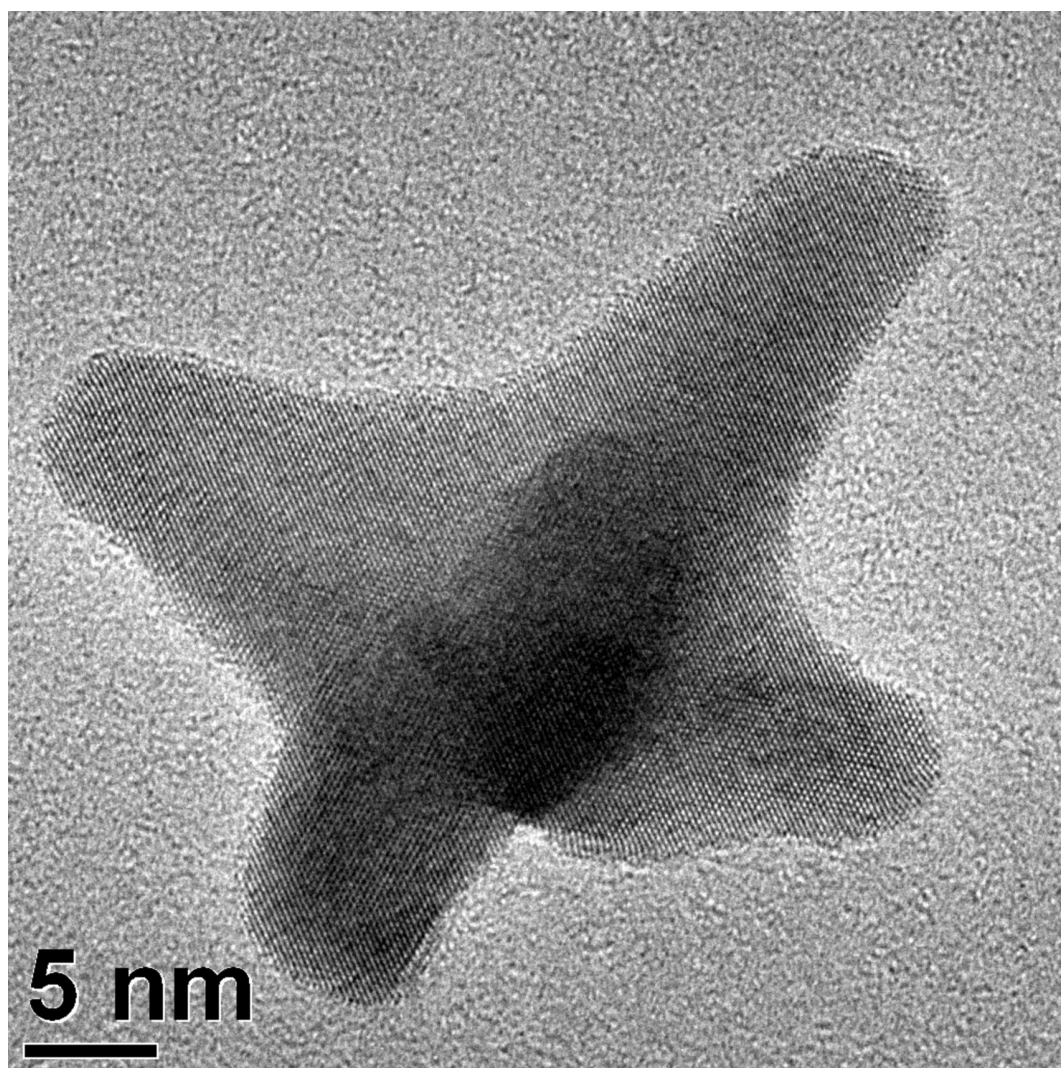


Figure S9c. HRTEM image of another typology **B** single crystal nanostar. The dark spot at the centre of the structure is a fifth branch pointing towards the observer. A sixth branch may be hidden behind the structure

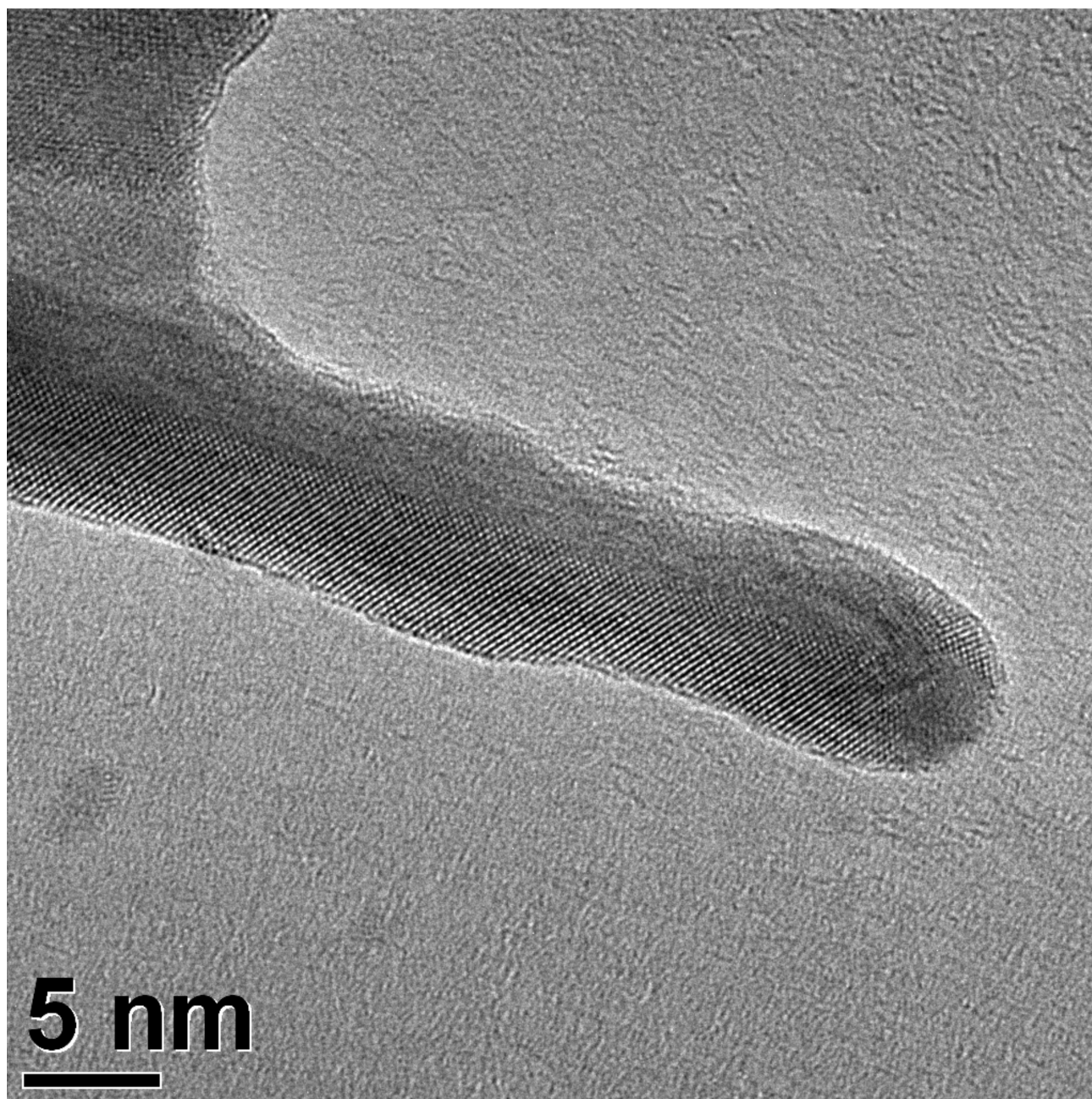


Figure S9d. Twinned gold branched nanoparticle (typology **C** objects). A detail of this image is reported in the main text as Figure 1 vii

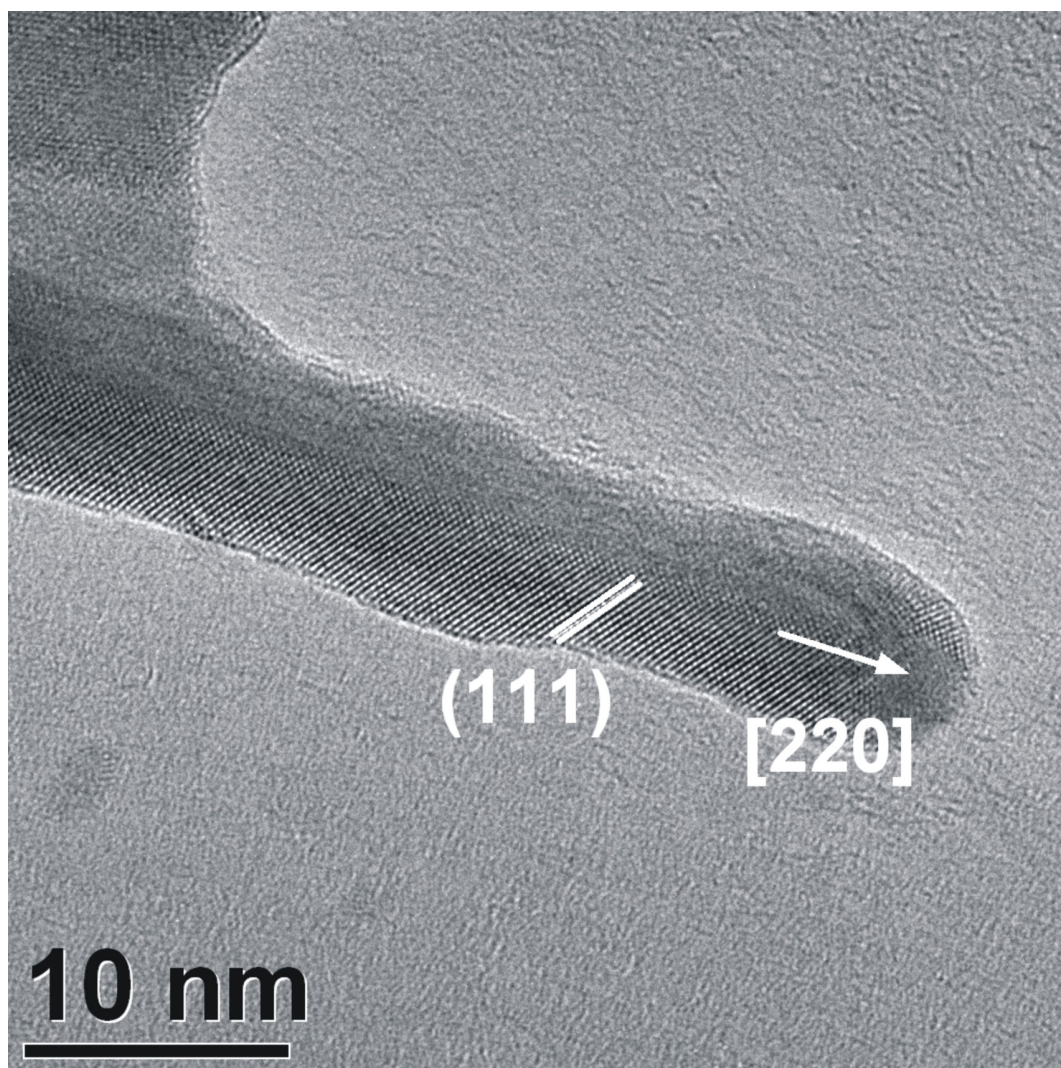


Figure S9e. Same as Figure S9d, with evidenced growth direction and one set of lattice planes.

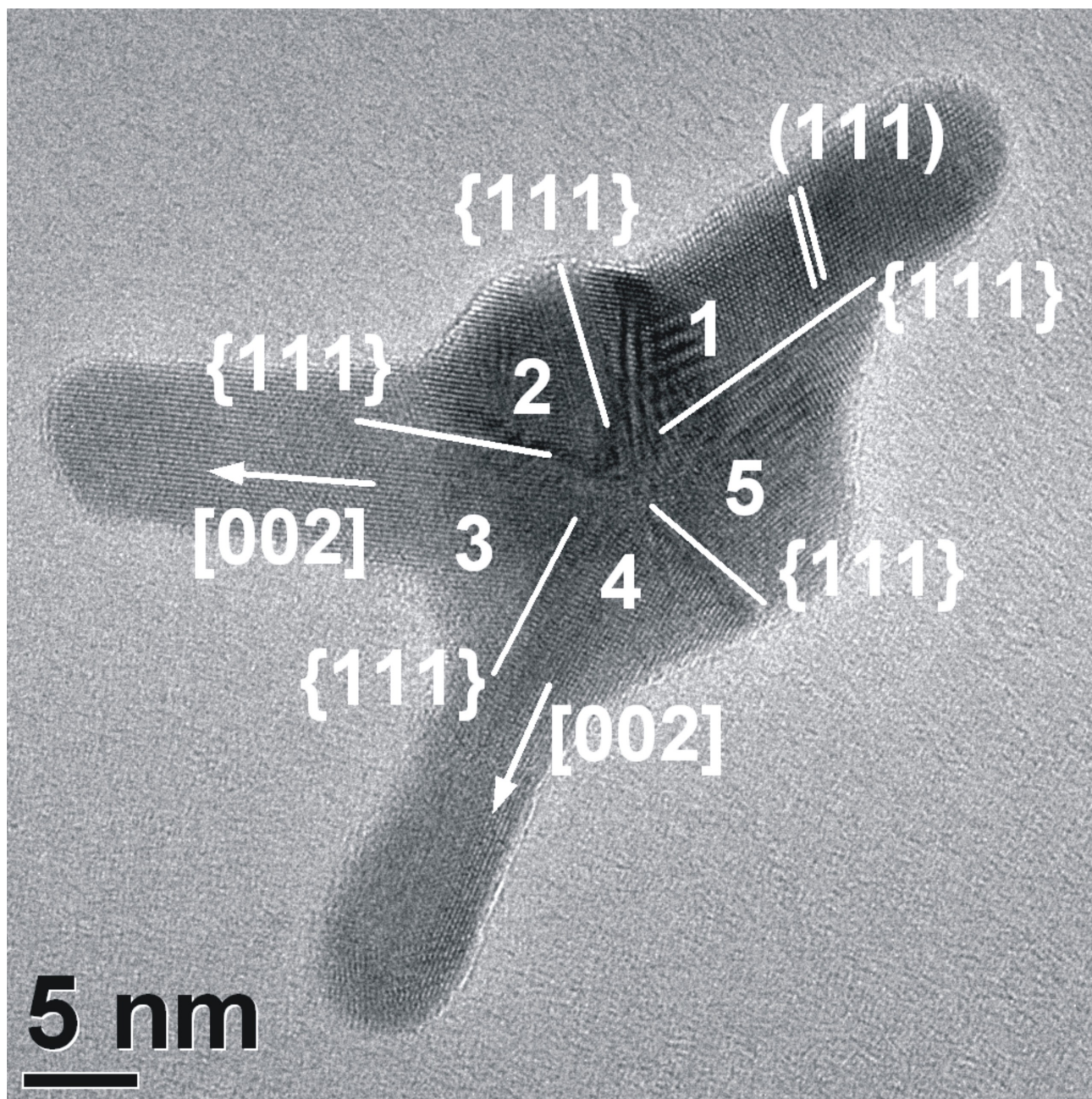
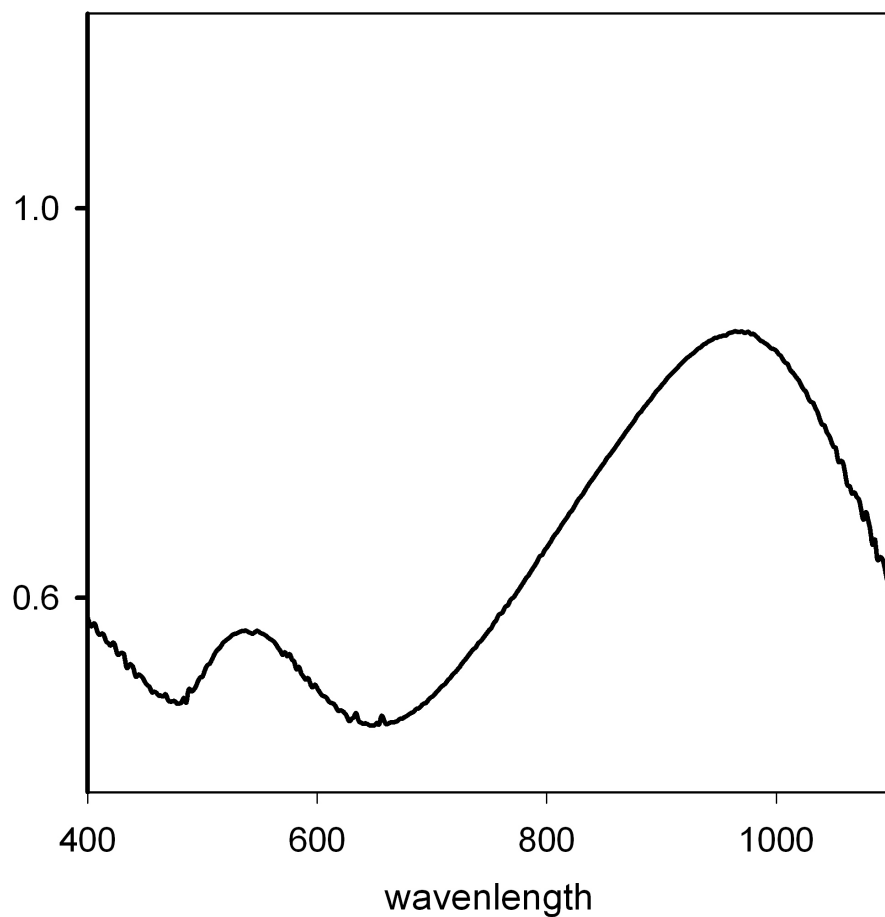


Figure S9f. HRTEM image of C-type branched asymmetric nanoparticle. The sets of both contact and lattice planes are reported, together with the most evident growth directions.

S10. Additional UV-Vis spectrum of a nanoobjects solution poor of type **B** objects (stars), from a 0.45 M LSB starting solution (400-1100 nm range)



S11. Variation of different parameters as a function of the LSB molarity added to the growth solution

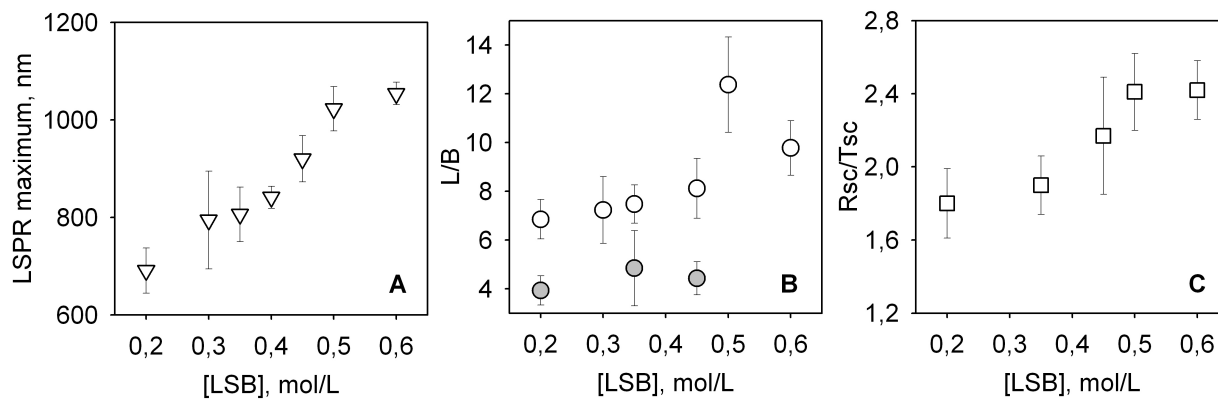


Figure S11. A: LSPR position. B: L/B for type **C** (white circles) and type **B** (grey circles) nano-objects. C: ratio of the rotational to the translational scattering amplitude in DLS